PCCP

PAPER

View Article Online
View Journal | View Issue

Cite this: *Phys. Chem. Chem. Phys.*, 2015, **17**, 5872

Investigating the role of human serum albumin protein pocket on the excited state dynamics of indocyanine green using shaped femtosecond laser pulses†

Muath Nairat,[a] Arkaprabha Konar,[a] Marie Kaniecki,[a] Vadim V. Lozovoy[a] and Marcos Dantus*[ab]

Received 30th October 2014,
Accepted 20th January 2015

DOI: 10.1039/c4cp04984e

www.rsc.org/pccp

Differences in the excited state dynamics of molecules and photo-activated drugs either in solution or confined inside protein pockets or large biological macromolecules occur within the first few hundred femtoseconds. Shaped femtosecond laser pulses are used to probe the behavior of indocyanine green (ICG), the only Food and Drug Administration (FDA) approved near-infrared dye and photodynamic therapy agent, while free in solution and while confined inside the pocket of the human serum albumin (HSA) protein. Experimental findings indicate that the HSA pocket hinders torsional motion and thus mitigates the triplet state formation in ICG. Low frequency vibrational motion of ICG is observed more clearly when it is bound to the HSA protein.

Introduction

A considerable amount of effort has been and is being made by both experimentalists and theoreticians on better understanding and modeling the early time dynamics of solvated molecules soon after photo-excitation, where the environment surrounding the molecules plays a major role in the ensuing molecular dynamics.[1–7] Understanding the quantum behavior of *cis–trans* isomerizing biomolecules is of even greater importance, given their paramount role in proper functioning of living beings.[8] Biological cavities formed primarily within protein pockets serve to direct and control the behavior of host molecules, their chemical reactivity and photochemical behavior. Studying probe-molecules confined by protein pockets can provide insight in to the interaction between host-molecules, intrinsic chromophores and drugs.[9–12] Furthermore, such understanding can be used to recognize the basis of pharmacokinetics and pharmacodynamics of protein-carried drugs,[13,14] wherein the chemical and physical properties of such confined molecules can differ drastically from those free in solution.[10] Development of effective protein fluorescent labels having specific targets,[15] and understanding the chemical behavior of the labeling ligand during the early stages of photoexcitation can be useful in gaining information about the ligand behavior inside the protein and in probing the stages of protein folding and different protein conformations as well.[16,17] One such case of special interest is how rhodopsin controls vision upon being excited by a photon. The absorption of photons trigger the isomerization of the bound 11-*cis*-retinal to produce the all-*trans* retinal, in turn initiating the process of vision.[18] Here we focus on indocyanine green (ICG) docked inside the pocket of human serum albumin (HSA) protein as a model system for studying the behavior of molecules confined in biological pockets.

Human serum albumin (HSA) protein is especially interesting as it is the most abundant protein in plasma and constitutes about half of human blood proteins. HSA plays a crucial role in the delivery and transport of many molecules and biomolecules such as fatty acids, drugs, metal ions and steroids within the body.[19] HSA consists of 585 amino acids forming a monomeric globular shape, which can be further divided into three α-helical domains.[20,21] Ligands bind with HSA either to the hydrophobic pocket of site IIA which is dominated by strong hydrophobic interactions, or to the polar cationic pocket of site IIIA which involves dipole–dipole, van der Waals and hydrogen bonding type of weak interactions.[9–11,22]

Indocyanine green (ICG) is a tricarbocyanine dye and is the only near-infrared FDA approved dye[23] that is widely used in a variety of medical applications such as cardio-circulatory measurements, liver function tests, ophthalmological imaging and sentinel lymph node mapping in cancer patients.[24–29] The spectroscopic properties of ICG have already been well investigated[30–33] and several photo-isomerization mechanisms were sought for ICG that address

[a] *Department of Chemistry, Michigan State University, East Lansing, Michigan 48824, USA. E-mail: dantus@msu.edu*
[b] *Department of Physics and Astronomy, Michigan State University, East Lansing, Michigan 48824, USA*

† Electronic supplementary information (ESI) available: ICG and ICG–HSA absorbance spectra, air saturated and Argon bubbled ICG and ICG–HSA integrated fluorescence intensity chirp dependence, and vibrational oscillations fitting parameters. See DOI: 10.1039/c4cp04984e

multiphoton processes to produce triplet state, photodegraded species and *cis* isomers.[34–36] Being a tricarbocyanine dye, ICG aggregation and photophysical behavior is highly dependent on the environment[31] and the molecule tends to exist in an all-*trans* form while in the ground state.[34,35] Moreover, the low fluorescence quantum yield for ICG in water ($\phi_F = 0.027$)[31] can be attributed to the excited state *trans–cis* isomerization,[37,38] large triplet state formation cross section[32] and several other photoreactions.[34–36] The main medical use of ICG arises from its ability to bind with albumin[39,40] and is therefore extensively used in the labeling of HSA.[41,42] ICG has a binding constant of 5.7×10^5 M^{-1} to HSA[43] and results in a bathochromic shift (red shift) of the ICG absorbance (ESI†, Fig. S1) which in turn increases the fluorescence quantum yield ($\phi_F = 0.040$).[31] Moreover, ICG exhibits a higher degree of photostability when forming J-aggregates, in non-polar solvents and in blood plasma.[44]

The asymmetric response of fluorescence intensity to negative and positive chirped pulses was first reported by Shank *et al.*[45] Fluorescence depletion for negatively chirped pulses was explained by an intrapulse pump–dump of the electronic population since the arrival order of frequencies is from high to low. This depletion has been used for controlling the population transfer in multilevel systems.[46–48] Various interpretations for the molecular response to chirped pulses have been proposed, Cao and coworkers[49] proposed an intrapulse three-level model, while Fainberg introduced non-Markovian relaxation into the existing theory.[50,51] More recently results from our research group showed that negative chirp is sensitive to intramolecular dynamics while positive chirp is sensitive to intermolecular dynamics.[52] When comparing a solution of IR144 in ethylene glycol, we noted that the negative chirp data was unaffected by temperature and a clear maximum depletion occurred at -2500 fs^2 corresponding to a pulse duration of 200 fs.[52] Maximum depletion depends on the optimum pulse duration and frequency sweep to dump population from the excited state. This occurs on a short timescale and is primarily dependent on the intramolecular potential energy surfaces. For positive chirps, however, temperature affected the chirp value when maximum fluorescence is achieved. The chirp values for maximum fluorescence ranged from 5000 to 10 000 fs^2, corresponding to dynamics occurring in the 0.5–1 ps timescales, which are associated with solvation dynamics.[52] Temperature affects viscosity and intermolecular dynamics associated with solvation. These changes are observed for positive chirps.

Here we used chirped femtosecond laser pulses to probe the early stages of excited state dynamical behavior of ICG molecules while free in solution and while confined inside HSA protein pocket. We also varied the repetition rate of the laser in order to probe the formation and dynamics of excited triplet states. In addition to using chirped pulses, we also performed pump–probe measurements to directly determine the timescales.

Experimental

The experimental setup (Fig. 1b) has been described previously,[52,53] wherein 38 fs pulses (when transform-limited) were produced from a regeneratively amplified Ti:Sapphire laser. The pulses were compressed and shaped using a MIIPS-HD (Biophotonic Solutions Inc.) phase and amplitude pulse shaper placed after the amplifier using the multiphoton intrapulse interference phase scan (MIIPS) approach.[54,55] Unfocused 90 μJ laser pulses centered at 800 nm at a repetition rate of 1 kHz or 200 Hz were used, with a peak intensity at the sample of 5×10^9 W cm^{-2} when transform limited. Chirped pulses having the phase function $\varphi(\omega) = 0.5\varphi''(\omega - \omega_0)^2$ were generated using the pulse shaper where φ'' is the quadratic phase. A typical chirp scan consisted of scanning the chirp from negative to positive 30 000 fs^2. Quadratic phase on a 38 fs transform limited (TL) pulse stretches it to longer durations according to $\tau/\tau_{TL} = \sqrt{1 + (4\ln 2)^2(\varphi''/\tau_{TL}^2)^2}$. The high frequency components (blue part of the pulse) arrive before the low frequency ones (red part of the pulse) for a negatively chirped pulse, while the order of arrival is reversed for a positively chirped pulse

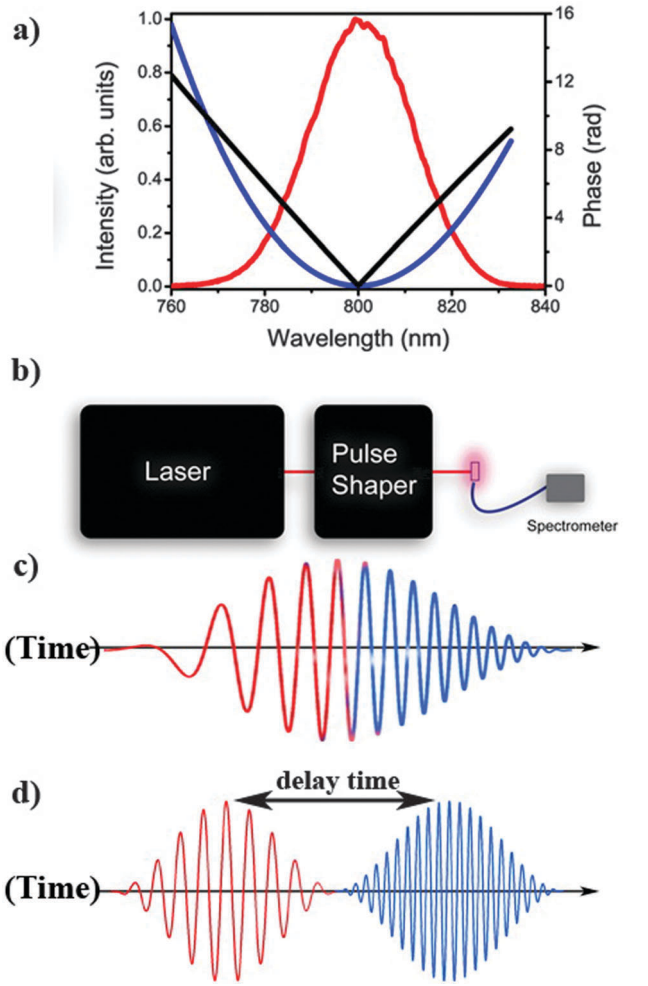

Fig. 1 (a) TL pulse spectrum (red) with positive chirp phase mask (blue) and positive delay time phase mask (black). (b) Experimental setup, note the laser was not focused on the cuvette. (c) Schematic representation of a positively chirped pulse in the time domain, and of a (d) pump–probe type pair of pulses with positive delay time having frequency arrival ordering such that the red portion of the pulse arrives before the blue portion.

(Fig. 1c), depending upon the magnitude of chirp or how "stretched" the pulse is. Dynamical information can be obtained by correlating the value of chirp to the pulse duration; for instance a chirp value of 1000 fs^2 can be used to observe processes occurring near 82 fs; the temporal stretching is determined by the formula given above. Repeated sets of measurements were taken over different days and compared and checked for reproducibility.

Delay time phase masks (Fig. 1a) were introduced using the shaper by delaying the red half (greater than 800 nm) of the pulse with respect to the blue half (smaller than 800 nm) by changing the slope of a linear phase. Delay scans were performed from negative to positive 1 ps in 20 fs steps. For negative time delays the pump pulse, consisting of the high frequency components, arrives before the low frequency ones, while for positive delays the lower frequency pulse precedes the higher frequency one (Fig. 1d). Integrated fluorescence signal was simultaneously detected at right angles using a compact spectrometer while ensuring that the collected signal is associated with the proper range for either ICG or ICG–HSA since ICG–HSA fluorescence occurs in a red shifted region compared to free ICG. Indocyanine green (Sigma-Aldrich, I2633) and human serum albumin protein (Sigma-Aldrich, A3782) were used as purchased without any further purification. 10 μM indocyanine green (ICG) and 1 : 1 × 10 μM indocyanine green with human serum albumin (ICG–HSA) solutions were freshly prepared and used immediately. All solutions were prepared under atmospheric conditions unless noted otherwise in the results section. Solutions were prepared in 10 mM, pH = 7 sodium phosphate buffer prepared using Milli-Q water and proper amounts of monosodium and disodium phosphate. Solutions were placed inside a 2 mm cuvette to minimize any possible phase distortion since accurate measurements are required while delivering dispersion free pulses with the exact desired delay times.

UV-visible (ATI/Unicam UV2) absorbance spectra for ICG and ICG–HSA were used to confirm ICG binding within the protein pocket (ESI†, Fig. S1) and check for ICG aggregation at the working concentration (ESI†, Fig. S2). Molecular docking was performed to simulate ICG conformation within the HSA pocket and to also determine the most favored binding site. The crystal structure of HSA was obtained from the protein data bank (PDB: 1AO6),[20] and the ICG 3D structure was created using ChemBio3D. HSA was loaded using AutoDock Tools,[56] water and multiple protein crystals were removed, polar hydrogen atoms were added, grid box size and position were assigned to contain all the protein and ICG rotatable bonds were identified using AutoDock Tools. The files were saved in proper formats and were docked using AutoDock Vina[57] which utilizes the Lamarckian Genetic Algorithm (LGA) based on the adaptive local method search and provides 10 conformers having the lowest binding energy. AutoDock Tools was used to visualize the docked ICG conformers; finally the ICG conformer with the lowest energy was further studied using a box of smaller grid size containing the docked position and was chosen to be visualized.

Results and discussion

1. Molecular modeling & docking

Molecular docking was performed for ICG molecule with HSA using AutoDock Vina to reveal the most favorable binding mode for ICG within HSA pocket and the most probable conformer while in the ground state. After visualizing the 10 most probable binding conformers and determining the one with the highest binding affinity, it was concluded that ICG is more likely to bind within the hydrophobic region of HSA (site IIA), presumably due to the hydrophobic nature of the majority of ICG molecule. Further docking was carried out in a smaller grid box which contained only site IIA of HSA pocket to identify the most favored ICG conformer inside that specific binding pocket. Visualization of the results for the conformer with the highest affinity is presented in Fig. 2. Note that ICG inside the HSA pocket is mostly in a *trans* configuration. The relatively tight configuration implies that the pocket provides some steric hindrance that may affect the photoisomerization behavior of ICG.

2. Fluorescence behavior with shaped laser pulses

Steady state absorption and fluorescence of ICG has been extensively discussed elsewhere;[31] here we investigate the use of shaped femtosecond pulses to probe the excited state dynamics of ICG and ICG–HSA especially during the first few hundreds femtoseconds after excitation.

Integrated fluorescence intensity from ICG and ICG–HSA solution as a function of spectral chirp (φ'') at repetition rates of 1 kHz (black) and 200 Hz (red) are shown in Fig. 3. The integrated intensity were collected for several measurements, compared without any normalization then finally averaged and normalized on a scale from 0 to 1. Notable differences were observed (Fig. 3a) in the fluorescence response 'chirp effect' curve for ICG at different repetition rates. At 200 Hz, a typical 'chirp effect' response is observed with fluorescence depletion for negatively chirped pulses followed by a rapid rise for positively chirped pulses. However, when operating at 1 kHz an additional fluorescence intensity decrease feature is observed around −5000 fs^2 which gets sharper upon approaching TL pulses. The rate of fluorescence increase for positive chirp is

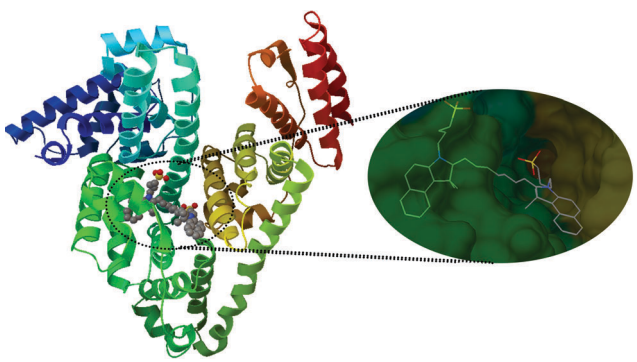

Fig. 2 Molecular modeling showing the most favored binding site of ICG within site IIA of the HSA protein. HSA was colored according to its chains and ICG elements were colored in grey (C), blue (N), yellow (S) and red (O).

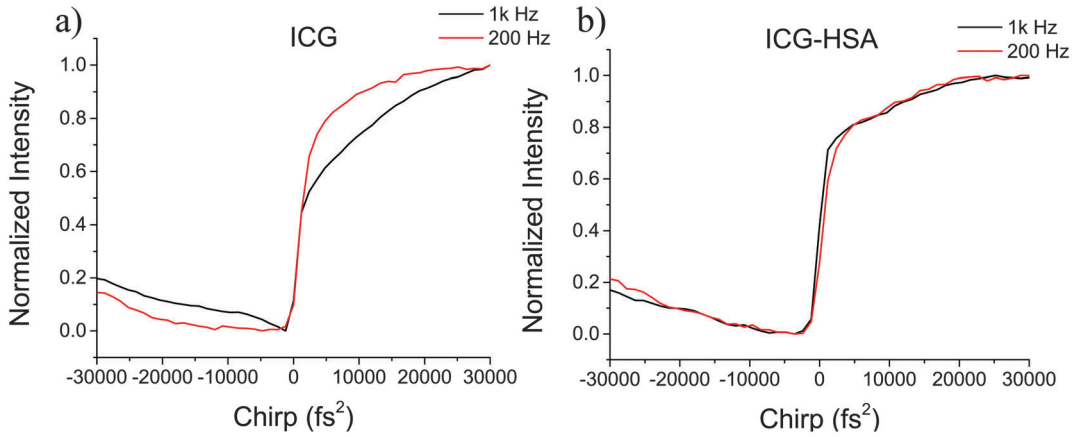

Fig. 3 Normalized integrated fluorescence intensity as a function of spectral chirp for (a) ICG solution and (b) ICG–HSA solution obtained at different repetition rates.

considerably slower when data is obtained at 1 kHz. Identical chirp effect curves are obtained for ICG–HSA (Fig. 3b) when collecting the fluorescence as a function of chirp at the two different repetition rates. From these experiments we learn that at 1 kHz ICG accumulates a transient species that is not present for ICG–HSA.

When comparing ICG and ICG–HSA results at 200 Hz, no difference in the dynamical behavior is observed when the data is normalized from 0 to 1 (Fig. 4a), confirming the absence of a transient species. When the data was normalized according to the fluorescence intensity for TL pulses (Fig. 4b), the fluorescence of ICG–HSA is less intense for positive chirps than that of free ICG.

Differences in the response to chirp due to the laser repetition rate are attributed to the photo-dynamical behavior of free ICG molecules in solution. Several single and multi-photon photo-isomerization pathways have been proposed to address the non-radiative behavior of ICG.[34–36] They can be summarized as excited state *trans–cis* isomerization, triplet state formation through intersystem crossing and formation of photo degradation products. ICG *cis* photo-isomer and triplet state have a lifetime of ~1 ms,[34] and thus can accumulate and be observed when the pulse repetition rate is 1 kHz, because consecutive pulses arrive at the sample every 1 ms. We confirmed the presence of triplet state by removing O_2, which acts as a triplet state quencher, from the sample by bubbling argon (Ar) in the solution and recording the chirp scans in the oxygen depleted samples. The fluorescence spectra for ICG solution bubbled with Ar as a function of chirp at 1 kHz (ESI†, Fig. S3) clearly shows a sharper decrease in the fluorescence intensity for negatively chirped pulses and slower rise for positively chirped pulses as compared to the air saturated solution. The accumulation of triplet ICG changes the observed behavior given that the signal arises from a different molecular species. Note that for ICG–HSA no such behavior was observed, even in the absence of oxygen using Ar bubbled solution (ESI†, Fig. S4). We conclude from this observation that the HSA protein pocket prevents the formation of the triplet state of ICG.

To get an even clearer picture and better understanding about the time scale of the relevant processes occurring during the chirp scan we performed pump probe type measurements as described in the experimental section on the same solutions. The detected fluorescence intensity normalized from 0 to 1 for

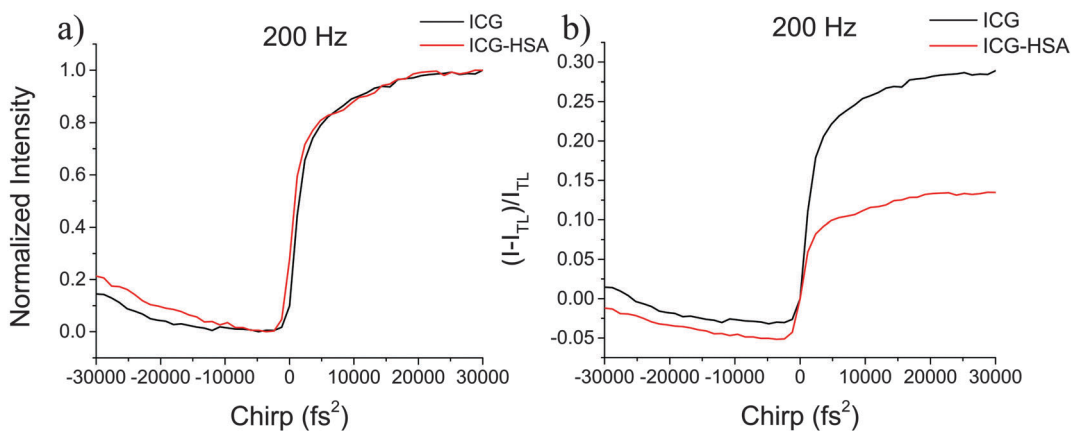

Fig. 4 Integrated fluorescence intensity as a function of spectral chirp at a repetition rate of 200 Hz for ICG (black) and ICG–HSA (red) normalized (a) from 0 to 1 and (b) normalized according to the integrated fluorescence when using TL pulses.

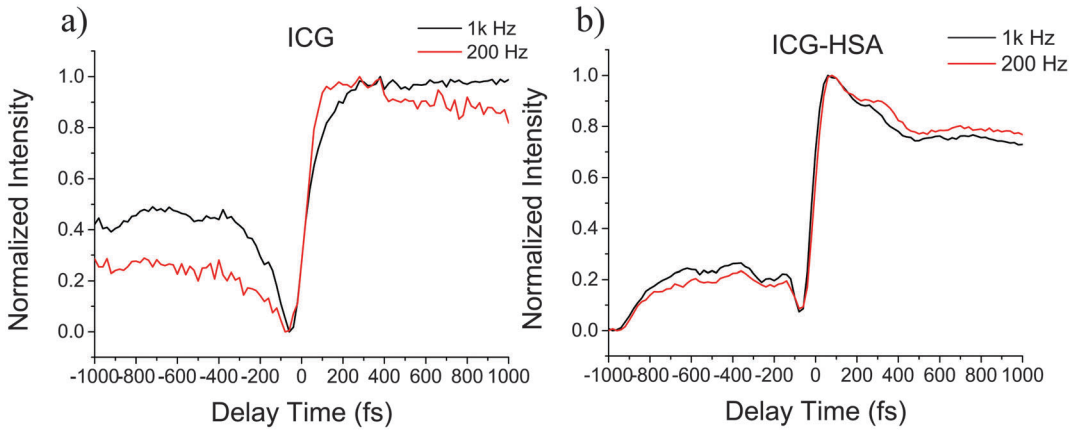

Fig. 5 Normalized integrated fluorescence intensity as a function of delay time between the pump and probe pulses for (a) ICG solution and (b) ICG–HSA solution at repetition rates of 1 kHz (black) and 200 Hz (red).

both ICG and ICG–HSA at different repetition rates are shown in Fig. 5(a) and (b) respectively. For negative delay times, lower fluorescence intensity was observed and this can be explained by stimulated depletion of the electronic population from the first excited state, while for positive delays, the order of arrival of the spectral parts of the pulse is reversed and is considered not suitable for dumping the electronic population back to the ground state.

We find that for ICG (Fig. 5a) at 1 kHz repetition rate compared with 200 Hz, there was a clear feature at negative delay times in fluorescence intensity from −400 fs to −50 fs. Additionally, with positive delay times, fluorescence intensity increases more slowly for the 1 kHz data. When ICG is confined inside the HSA pocket no difference can be seen between the 1 kHz and 200 Hz time-resolved curves (Fig. 5b). The time resolved data again point to the accumulation of triplet-state ICG when the experiments are performed at 1 kHz, and we also confirm that the HSA pocket prevents the formation of triplet-state ICG.

The fluorescence intensity as a function of delay time (Fig. 5b) for ICG–HSA reveals ∼290 fs vibrational oscillations in the negative delay portion of the transient and ∼175 fs vibrational oscillations in the positive delay portion. These oscillations are not observed for free ICG. Fitting the vibrational oscillations observed for ICG–HSA to a cosine function of the form $A + a\cos(2\pi\omega t + \phi) + bt$ (detailed fit parameters can be found in ESI†, Table S1) (Fig. 6) yields a vibrational frequency of 115 ± 15 cm^{-1} and 190 ± 15 cm^{-1} for the negative and positive delay times respectively. These values are slightly different from previously reported vibrational frequency of ICG in methanol (146 cm^{-1} for the ground-state bleach and 138 cm^{-1} for the excited state stimulated emission).[58] While our experiments are carried out in aqueous solutions, and our signal to noise is low, the significant differences can be attributed to the presence of ICG inside the HSA binding pocket.

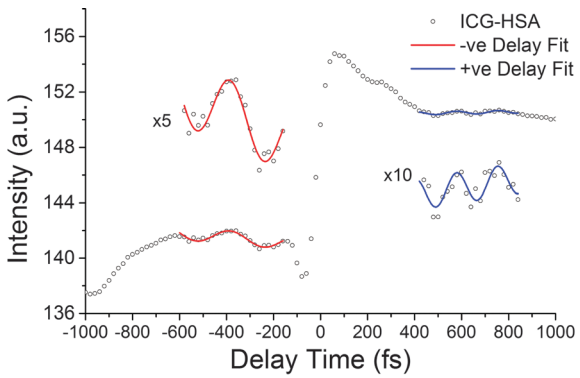

Fig. 6 Integrated fluorescence intensity as a function of delay time between pump and probe pulses for ICG–HSA. The ∼290 fs oscillations in the negative delay time side and the ∼175 fs oscillations in the positive delay time were fitted using a cosine function with 115 ± 15 cm^{-1} and 190 ± 15 cm^{-1} oscillation respectively and are vertically zoomed in the insets.

Conclusions

The early, sub-picosecond, excited state dynamics of indocyanine green in aqueous solution as well as within the hydrophobic pocket of human serum albumin were studied using both chirped femtosecond laser pulses and pump–probe time-resolved measurements. In general, the behavior of indocyanine green in solution is similar to that of other cyanine dyes.[52] When aqueous solution experiments are carried out at high repetition rates it becomes clear that a new molecular species accumulates and different photodynamic behavior is observed. The differences are assigned to the accumulation of triplet state. We confirmed the nature of the triplet state by carrying out experiments in the absence of oxygen, an effective triplet quencher. When the probe molecule is inside the protein pocket, no triplet state formation and accumulation is detected. Time resolved experiments confirm the chirped pulse experiments and reveal coherent vibrational oscillations when the probe molecule is inside the protein pocket.

Acknowledgements

We would like to thank Prof. Warren F. Beck for his valuable insights regarding triplet state formation and general discussion about excited state dynamics. Also we thank Dr Rachel Glenn for her valuable contribution to this work.

References

1 W. P. de Boeij, M. S. Pshenichnikov and D. A. Wiersma, *Annu. Rev. Phys. Chem.*, 1998, **49**, 99–123.
2 A. Yu, C. A. Tolbert, D. A. Farrow and D. M. Jonas, *J. Phys. Chem. A*, 2002, **106**, 9407–9419.
3 R. Jimenez, G. R. Fleming, P. V. Kumar and M. Maroncelli, *Nature*, 1994, **369**, 471–473.
4 G. R. Fleming and M. Cho, *Annu. Rev. Phys. Chem.*, 1996, **47**, 109–134.
5 E. T. J. Nibbering, D. A. Wiersma and K. Duppen, *Phys. Rev. Lett.*, 1992, **68**, 514–517.
6 S. Mukamel, *Annu. Rev. Phys. Chem.*, 2000, **51**, 691–729.
7 N. Nandi, K. Bhattacharyya and B. Bagchi, *Chem. Rev.*, 2000, **100**, 2013–2046.
8 C. Dugave and L. Demange, *Chem. Rev.*, 2003, **103**, 2475–2532.
9 D. Zhong, A. Douhal and A. H. Zewail, *Proc. Natl. Acad. Sci. U. S. A.*, 2000, **97**, 14056–14061.
10 C. Martín, M. Gil, B. Cohen and A. Douhal, *Langmuir*, 2012, **28**, 6746–6759.
11 C. Martin, B. Cohen, I. Gaamoussi, M. Ijjaali and A. Douhal, *J. Phys. Chem. B*, 2014, **118**, 5760–5771.
12 S. H. Gellman, *Chem. Rev.*, 1997, **97**, 1231–1734.
13 U. Kragh-Hansen, *Pharmacol. Rev.*, 1981, **33**, 17–53.
14 T. Peters, Jr., *Adv. Protein Chem.*, 1985, **37**, 161–245.
15 M. S. T. Gonçalves, *Chem. Rev.*, 2008, **109**, 190–212.
16 N. Mataga, H. Chosrowjan and S. Taniguchi, *J. Photochem. Photobiol., C*, 2004, **5**, 155–168.
17 C. A. Royer, *Chem. Rev.*, 2006, **106**, 1769–1784.
18 G. Wald, *Science*, 1968, **162**, 230–239.
19 T. Peters, Jr., *All about Albumin: Biochemistry, Genetics, and Medical Applications*, Academic Press, San Diego, 1996.
20 S. Sugio, A. Kashima, S. Mochizuki, M. Noda and K. Kobayashi, *Protein Eng.*, 1999, **12**, 439–446.
21 X. M. He and D. C. Carter, *Nature*, 1992, **358**, 209–215.
22 Y. V. Il'ichev, J. L. Perry and J. D. Simon, *J. Phys. Chem. B*, 2002, **106**, 452–459.
23 J. Bongsu, V. I. Vullev and B. Anvari, *IEEE J. Quantum Electron.*, 2014, **20**, 149–157.
24 J. V. Frangioni, *Curr. Opin. Chem. Biol.*, 2003, **7**, 626–634.
25 L. A. Yannuzzi, *Am. J. Ophthalmol.*, 2011, **151**, 745–751.
26 H. Nimura, N. Narimiya, N. Mitsumori, Y. Yamazaki, K. Yanaga and M. Urashima, *Br. J. Surg.*, 2004, **91**, 575–579.
27 B. E. Schaafsma, J. S. D. Mieog, M. Hutteman, J. R. van der Vorst, P. J. K. Kuppen, C. W. G. M. Löwik, J. V. Frangioni, C. J. H. van de Velde and A. L. Vahrmeijer, *J. Surg. Oncol.*, 2011, **104**, 323–332.
28 J. R. van der Vorst, B. E. Schaafsma, F. P. R. Verbeek, R. J. Swijnenburg, M. Hutteman, G. J. Liefers, C. J. H. van de Velde, J. V. Frangioni and A. L. Vahrmeijer, *Br. J. Dermatol.*, 2013, **168**, 93–98.
29 T. Desmettre, J. M. Devoisselle and S. Mordon, *Surv. Ophthalmol.*, 2000, **45**, 15–27.
30 M. L. Landsman, G. Kwant, G. A. Mook and W. G. Zijlstra, *J. Appl. Physiol.*, 1976, **40**, 575–583.
31 R. Philip, A. Penzkofer, W. Bäumler, R. M. Szeimies and C. Abels, *J. Photochem. Photobiol., A*, 1996, **96**, 137–148.
32 S. Reindl, A. Penzkofer, S. H. Gong, M. Landthaler, R. M. Szeimies, C. Abels and W. Bäumler, *J. Photochem. Photobiol., A*, 1997, **105**, 65–68.
33 F. Rotermund, R. Weigand, W. Holzer, M. Wittmann and A. Penzkofer, *J. Photochem. Photobiol., A*, 1997, **110**, 75–78.
34 H. Gratz, A. Penzkofer, C. Abels, R. M. Szeimies, M. Landthaler and W. Bäumler, *J. Photochem. Photobiol., A*, 1999, **128**, 101–109.
35 M. Fuyuki, K. Furuta and A. Wada, *J. Photochem. Photobiol., A*, 2013, **252**, 152–158.
36 M. Fuyuki, K. Furuta and A. Wada, *RSC Adv.*, 2013, **3**, 7313–7320.
37 P. K. Sudeep, K. Takechi and P. V. Kamat, *J. Phys. Chem. C*, 2006, **111**, 488–494.
38 Y. H. Meyer, M. Pittman and P. Plaza, *J. Photochem. Photobiol., A*, 1998, **114**, 1–21.
39 T. J. Muckle, *Biochem. Med.*, 1976, **15**, 17–21.
40 C. Colyer, *Cell Biochem. Biophys.*, 2000, **33**, 323–337.
41 E. D. Moody, P. J. Viskari and C. L. Colyer, *J. Chromatogr. B: Biomed. Sci. Appl.*, 1999, **729**, 55–64.
42 E. M. McCorquodale and C. L. Colyer, *Electrophoresis*, 2001, **22**, 2403–2408.
43 M. Y. Berezin, K. Guo, W. Akers, J. Livingston, M. Solomon, H. Lee, K. Liang, A. Agee and S. Achilefu, *Biochemistry*, 2011, **50**, 2691–2700.
44 W. Holzer, M. Mauerer, A. Penzkofer, R. M. Szeimies, C. Abels, M. Landthaler and W. Bäumler, *J. Photochem. Photobiol., B*, 1998, **47**, 155–164.
45 G. Cerullo, C. J. Bardeen, Q. Wang and C. V. Shank, *Chem. Phys. Lett.*, 1996, **262**, 362–368.
46 C. J. Bardeen, V. V. Yakovlev, K. R. Wilson, S. D. Carpenter, P. M. Weber and W. S. Warren, *Chem. Phys. Lett.*, 1997, **280**, 151–158.
47 J. S. Cao, C. J. Bardeen and K. R. Wilson, *Phys. Rev. Lett.*, 1998, **80**, 1406–1409.
48 C. J. Bardeen, J. Cao, F. L. H. Brown and K. R. Wilson, *Chem. Phys. Lett.*, 1999, **302**, 405–410.
49 J. Cao, J. Che and K. R. Wilson, *J. Phys. Chem. A*, 1998, **102**, 4284–4290.
50 B. D. Fainberg and V. A. Gorbunov, *J. Chem. Phys.*, 2002, **117**, 7222–7232.
51 B. D. Fainberg and V. A. Gorbunov, *J. Chem. Phys.*, 2004, **121**, 8748–8754.
52 A. Konar, V. V. Lozovoy and M. Dantus, *J. Phys. Chem. Lett.*, 2014, **5**, 924–928.
53 A. Konar, V. V. Lozovoy and M. Dantus, *J. Phys. Chem. Lett.*, 2012, **3**, 2458–2464.
54 B. Xu, J. M. Gunn, J. M. D. Cruz, V. V. Lozovoy and M. Dantus, *J. Opt. Soc. Am. B*, 2006, **23**, 750–759.
55 Y. Coello, V. V. Lozovoy, T. C. Gunaratne, B. Xu, I. Borukhovich, C.-h. Tseng, T. Weinacht and M. Dantus, *J. Opt. Soc. Am. B*, 2008, **25**, A140–A150.
56 M. F. Sanner, *J. Mol. Graphics Modell.*, 1999, **17**, 57–61.
57 O. Trott and A. J. Olson, *J. Comput. Chem.*, 2010, **31**, 455–461.
58 J.-S. Park and T. Joo, *J. Chem. Phys.*, 2002, **116**, 10801–10808.